Composites Part B 135 (2018) 119–128

Contents lists available at ScienceDirect

Composites Part B

journal homepage: www.elsevier.com/locate/compositesb

Microwave absorption properties of holey graphene/silicone rubber composites

Chun-Yu Chen [a, b], Nen-Wen Pu [a, *], Yih-Ming Liu [c], Li-Hang Chen [c], Chia-Hung Wu [d], Tsai-Yi Cheng [a], Ming-Hsien Lin [c], Ming-Der Ger [c, **], Yann-Jang Gong [b], You-Yu Peng [b], Peter M. Grubb [e], Ray T. Chen [e]

[a] Department of Photonics Engineering, Yuan Ze University, Zhongli, Taoyuan 320, Taiwan
[b] Chemical System Research Division, National Chung Shan Institute of Science and Technology, Longtan, Taoyuan 325, Taiwan
[c] Department of Chemical & Materials Engineering, Chung Cheng Institute of Technology, National Defense University, Dasi, Taoyuan 335, Taiwan
[d] School of Defense Science, Chung Cheng Institute of Technology, National Defense University, Dasi, Taoyuan 335, Taiwan
[e] Department of Electrical and Computer Engineering, University of Texas, Austin, TX 78701, USA

ARTICLE INFO

Article history:
Received 16 June 2017
Received in revised form
16 September 2017
Accepted 1 October 2017
Available online 7 October 2017

Keywords:
Silicone rubber composite
Holey graphene
Microwave absorption
Low filler loading

ABSTRACT

The complex permittivity and return loss (RL) for the composites of silicone rubber filled with holey graphene nanosheets (HGNS, prepared by ultra-rapid heating during the step of thermal reduction/exfoliation of graphite oxide) were measured in the 3–18 GHz range. HGNS-based composites were found to have significantly higher microwave absorption than composites incorporating other types of graphene reduced at lower heating rates. Even with only 1 wt.% loading, its experimentally measured RL reached −32.1 dB at 13.2 GHz with a thickness of 2 mm, and simulation suggested that at a thickness of 3 mm its RL can be as low as −45.3 dB at 7.8 GHz. Material characterization indicated that the density of the holes increased with the temperature ramp rate, and the hole sizes ranged from 5 to 300 nm. Compared to other graphene samples, HGNS possessed significantly larger specific surface area and higher density of defects, suggesting that defect-induced losses, interfacial polarization, and multiple reflection/scattering at the interfaces are the major loss mechanisms. Our simple and low-cost process as well as the very low loading ratio of HGNS are advantageous for cost reduction in future applications.

1. Introduction

Due to their wide applications in consumer electronics, communication devices, and stealth technology, extensive studies have been carried out on the development of microwave absorbers and shields [1–13]. There have also been wide studies on polymer-based composites containing microwave-absorbing carbon ingredients, such as carbon black, graphite, expanded graphite, carbon fiber, CNTs, and graphene (or reduced graphene oxide, RGO) [14–34]. These efforts have been motivated by their advantages of high absorption ability, wide band, light weight, thinness, flexibility, low cost, and stable thermal and chemical properties. In particular, carbon nanotubes (CNTs) [18–20,24] and graphene [12,13,21–25,30–34] have the greatest potential as high-performance absorbing materials owing to their many desirable properties, including unique geometry effects, high specific surface area, and high conductivity. In 2008, Liang et al. [31] first reported a microwave shielding effectiveness of 21 dB at 8.2 GHz in epoxy composites filled with 15 wt.% of graphene. In 2011, Bai et al. [21] and Wang et al. [22] separately discovered that graphene could also provide remarkable microwave absorption. Subsequently, Bhattacharya et al. [24] found that graphene can offer higher microwave absorption than CNT, and Wen et al. [32] reported that RGO outperforms graphite nanoplatelets in microwave shielding. To explain why graphene is superior to other nano-carbon microwave absorbers, some researchers proposed that graphene has a unique loss mechanism: multiple reflections from the dihedral angle formed between neighboring graphene sheets [21,23] and multiple scattering from the corrugated graphene surfaces [32]. Recently we have reported that well-dispersed, highly exfoliated graphene is capable of providing excellent microwave absorption

* Corresponding author.
** Corresponding author.
E-mail addresses: nwpuccit@saturn.yzu.edu.tw (N.-W. Pu), mingderger@gmail.com (M.-D. Ger).

https://doi.org/10.1016/j.compositesb.2017.10.001
1359-8368/

(−37.8 dB at 12.3 GHz) at very low loading of 1 wt.% [30]. Additional studies on the temperature-dependent microwave shielding [33] and absorption [34] performances of graphene have confirmed its usefulness at elevated temperatures. Combinations of graphene with other dielectric or magnetic nano-fillers, such as CNTs [25], Fe_3O_4 [35], hematite [36], α-Fe [37], CuS [38], Ni [39], and $NiFe_2O_4$ [40], have also been demonstrated. These hybrid fillers have exhibited improved microwave absorption compared to pure graphene. Here we present a study on the extraordinary microwave absorption performances of *holey* graphene—a new type of graphene full of holes, which can considerably affect its electromagnetic properties.

Due to its two-dimensional (2-D) geometry, graphene easily restacks during the fabrication process in many applications and thus loses its exceptional physical properties to a great extent. For example, restacking of graphene leads to lower capacity and rate capability in applications of Li ion batteries (LIBs) [41–43] and supercapacitors (SCs) [44]. Therefore, creating anti-restacking 3-dimensional (3-D) structures [45–54] is important for realizing the full advantage of graphene. Researchers have reported excellent microwave absorption properties of many well-designed 3-D porous materials, which have complicated structures and anti-restacking capability. For example, hierarchical porous ZnO flowers [55], hollow porous Ni/SnO_2 hybrids [56], hierarchical hollow CuS microspheres [57], ordered honeycomb SnO_2 foams [58], flower-like CuS hollow microspheres composed of nanoflakes [59], yolk–shell structured composites [60,61], 3-D free-standing graphene foam [62], and graphene/polymer foam [63] have been successfully synthesized and their superior microwave absorption/shielding properties have been demonstrated.

Alternatively, we have found that creating a holey structure on graphene nanosheets with outward-opening hole edges and a significantly roughened surface morphology resulted in good resistance to restacking [44]. Using such kind of holey graphene, improvements in the performances of LIBs [64–67] and SCs [44,68,69] have been achieved because the holes offer shortcuts for the ions to diffuse rapidly into the interlayer space. Several methods have been proposed to produce holey graphene by different research groups [64–71], and studies on its applications to LIBs and SCs have been reported recently. Another unique feature of holey graphene is the high density of defects around the hole edges, which can serve as active sites for capturing extra Li ions and thus improve the electrochemical properties of LIBs [72,73]. These defects can equally play an important role in microwave absorption according to many previous studies [22,33,35,36,74–76]. The attractive properties of holey graphene—the anti-restacking ability and high defect density—suggest that it should be very suitable for the application in microwave absorption as well. We demonstrate here the excellent microwave absorbing performance of holey graphene produced by an ultra-rapid heating method.

2. Experimental details

2.1. Materials

The starting material for the production of graphene nanosheets (GNS) and holey graphene nanosheets (HGNS) was natural graphite powder (200 mesh, or particle sizes $\leq$ 74 μm, acquired from Alfa Aesar), which has 99.9995% purity and 2.25 g/cm^3 density.

The silicone rubber (Momentive, RTV-615A and B) was a two-component (base A and curative B) liquid product, which cures by mixing the base and the curative in a 10:1 wt ratio. The curing takes 24 h at 25 °C to permit handling, but the time can be shortened considerably by heating.

2.2. Preparation of GNSs with various heating rates

Natural graphite was oxidized by the Staudenmaier method to form graphite oxide (GO). The GO powder was then thermally reduced/exfoliated into various kinds of GNSs (or RGO) by heating to 300 °C in an air-filled quartz tube at different temperature ramp rates. The GNS samples prepared at temperature ramp rates of 1, 10, and 30 °C/min were named GNS300-1, GNS300-10, and GNS300-30, respectively.

2.3. Preparation of HGNS

The HGNS sample was obtained using an ultra-rapid heating method [44]. To achieve an extremely high temperature ramp rate, GO powder was dumped onto the central zone of the quartz tube surface preheated to 300 °C using a long metal tool, and instantaneously reduced/exfoliated into HGNS. An ultra-high temperature ramp rate of about 100 °C/s (6000 °C/min) was achieved by this means, and the GO was rapidly reduced while CO_2 gas was generated between neighboring layers much faster than it could escape. The huge pressure not only exfoliated the layers but also created numerous holes at weak spots in the graphene sheets.

2.4. Material analysis

Observation of the morphology of the GNS and HGNS samples was carried out using a scanning electron microscope (SEM, Hitachi, S-3000N) and a transmission electron microscope (TEM, FEI, Tecnai G2 F30). X-ray diffractometry (XRD, Rigaku D/Max 2200) was utilized to examine the crystal structure of graphene. Furthermore, a Renishaw inVia Raman Microscope was used to characterize the D and G bands of GNS and HGNS samples. Nitrogen adsorption isotherms were measured at 77 K with a Micromeritics ASAP 2010 Surface Area and Porosity Analyzer to determine the Brunauer-Emmett-Teller (BET) specific surface area (SSA) for GNS and HGNS samples. We also employed elemental analysis (EA, Thermo Scientific, Flash EA2000 CHNS/O Analyzer) for analyzing the O and C atomic contents of the GNSs and HGNS.

2.5. Preparation of the microwave absorbing composite sheets

Uniform dispersion of graphene in the matrix is of utmost importance for maximizing the performance of the composite. Premixing using a planetary mixer in combination with repetitive calendering (three roll milling) was employed to ensure a high degree of graphene dispersion. A planetary centrifugal mixer (Thinky, AR-250) was employed in premixing graphene (GNS300-1, GNS300-10, GNS300-30, or HGNS) powder with silicone rubber base (RTV-615A) for 10 min before degassing for 5 min. Once premixing was complete, the viscous solution was further mixed by a three roll mill (Exakt, 80E). This was repeated 9 times so that uniform dispersion of GNS or HGNS could be attained. The angular speed ratio of the three rollers was 1:3:9, with adjacent rollers rotating in the opposite directions. Agglomerates were effectively ripped apart by the large shear forces created by the speed differences of rollers. To ensure uniform distribution of graphene fillers throughout the matrix, the gaps at the front (between the 1st and 2nd roller) and at the rear (between the 2nd and 3rd rollers) were gradually reduced to 35 μm and 25 μm, respectively, down from original 90 μm and 80 μm. Finally, the curative (RTV-615B) was added and the mixture was further mixed by the planetary mixer for an additional 5 min and then degassed for 2.5 min.

With the curative and graphene fully dispersed in the base, the liquid mixture was ready to be shaped. This was accomplished by pouring the viscous mixture into a 16 cm × 16 cm panel mold 2 mm

thick. To effectively shorten the vulcanization time for silicone rubber, the composite was cured at 120 °C, under pressure of 3 MPa, for 1 h in a hot compression machine. This 1-wt.% GNS/ or HGNS/ silicone rubber composite absorber sheet was then trimmed to 15 cm × 15 cm, which was the required dimensions of the microwave absorber sheet for the EM characterization system.

2.6. Characterization of EM properties

A free-space microwave measurement (FSMM) system [30,77,78] was adopted for the characterization of EM properties of the composite absorbers. In the FSMM setup, a microwave propagating in free space was emitted and received by two horn antennas. The complex permittivity and permeability from 3 to 18 GHz were extracted from the S-parameters measured with a vector network analyzer (Agilent, PNA E8362B, 10 MHz - 20 GHz).

Compared to waveguide- or transmission-line-based systems there are several advantages to an FSMM geometry. Most importantly, it is difficult to achieve a seamless contact necessary to prevent air gaps and subsequent losses of measurement accuracy for waveguide- or coaxial-transmission-line-based measurement. By contrast, as a non-contact method, FSMM is less stringent in sample preparation requirement, facilitating more reliable and reproducible results.

Our FSMM system was utilized not only to measure the permittivity and permeability of the sample, but also to directly obtain the value of return loss (RL), which is the key indicator of microwave-absorbing performance. In the RL measurements, the absorber sheet under test was mounted onto an aluminum plate. All the measurements were performed at room temperature.

3. Results and discussion

3.1. Material characteristics of GNSs and HGNS

The SEM micrographs showing the morphology of the graphene samples (GNS300-1, GNS300-10, GNS300-30, and HGNS300) are displayed in Fig. 1. Evidently the number and size of holes on the graphene surface increased as the heating rate was raised. Rather flat and smooth surface morphology are observed for GNS300-1 (Fig. 1 (a)). As the heating rate increased, the morphology roughened and the volume expanded due to exfoliation. When the heating rate was increased to 30 °C/min (Fig. 1 (c)), small holes started to appear on the graphene surface. Ultimately, when the GO was exfoliated at the maximum achievable heating rate (HGNS300), the largest amount of holes with the largest sizes (5–300 nm) were created (Fig. 1(d) and (e)). This result indicates that the heating rate of the exfoliation process significantly affects the hole formation. This phenomenon can be explained by the mechanism of the thermal reduction/exfoliation of GO. There are many defective regions which have lower mechanical strength than other areas on the GO sheets due to severe oxidation and chemical reaction [79]. Therefore, when the GO was heated up to the target temperature ultra-rapidly (about 6000 °C/min), the gas produced from the decomposition of functional groups built up a high pressure, which punched the defective sites and created through-holes. The magnified SEM image in Fig. 1(e) clearly showed that the edges of these holes opened outward (see the red circles), which supports this mechanism. Such a protruding-edge structure can effectively prevent face-to-face restacking of the exfoliated sheets during the subsequent manufacturing of microwave-absorbing sheets. In addition, HGNS300 in Fig. 1(e) showed much rougher surface morphology, which can also alleviate the restacking problem. This anti-restacking property of HGNS300 is beneficial for enhancing the microwave absorption performance, as will be discussed in Sec 3.3.

The degree of exfoliation and crystallinity of HGNS could be characterized by XRD. In Fig. 2, natural graphite with a typical interlayer space of 0.34 nm exhibited a sharp (002) peak at $2\theta = 26.5°$. After oxidation, the GO sample showed a characteristic peak at a much smaller 2θ angle of 11.5°, which corresponded to a significantly enlarged interlayer distance from 0.34 to 0.78 nm due to the formation of oxygen functional groups between graphite layers. For GNS300-1, GNS300-10, GNS300-30, and HGNS300, the (002) peak disappeared totally as a result of a high degree of exfoliation after the thermal exfoliation/reduction of GO.

TEM images of the GNS and HGNS samples are shown in Fig. 3. All samples exhibited the distinct feature of numerous wrinkles common to all thermally exfoliated Staudenmaier graphene. GNS300-1, which was reduced at the lowest heating rate, was very

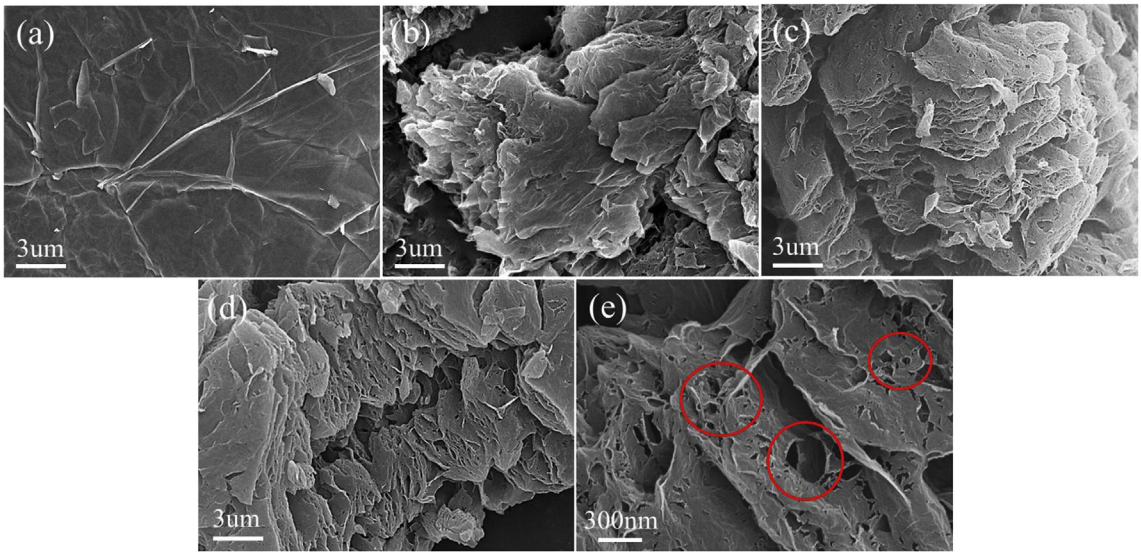

Fig. 1. SEM images of (a) GNS300-1, (b) GNS300-10, (c) GNS300-30, and (d) HGNS300. (e) High-magnification image of the HGNS300 sample (the red circles reveal the outward-opening edges of the holes). (For interpretation of the references to colour in this figure legend, the reader is referred to the web version of this article.)

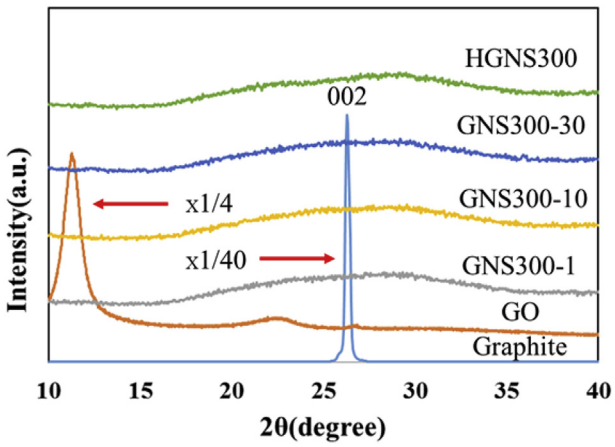

Fig. 2. The XRD patterns of graphite (×1/40), GO (×1/4), GNS300-1, GNS300-10, GNS300-30, and HGNS300.

poorly exfoliated, as shown in Fig. 3(a). As the heating rate increased, the image transparency increased, indicating a higher degree of exfoliation. The number of holes on graphene also increased with increasing heating rate: GNS300-1 and GNS300-10 were basically non-holey; GNS300-30 started to show signs of holes; and HGNS300 showed unambiguously the presence of numerous holes (the red circles indicate the areas containing holes). The TEM image for HGNS300 revealed that its hole sizes can be as small as ~5 nm.

Fig. 4 displays the high-resolution (HR) TEM image of HGNS300. There are 4–5 layers in this holey graphene, determined from the lattice fringes (indicated by the red lines) at the folded edges. The inset in Fig. 4 shows the spacing (0.34 nm) between atomic layers.

Raman analysis was employed to further investigate the structure of the GNSs and HGNS. The in-plane vibration of graphitic lattice correlates with the G band, whereas the D band is associated with the disorders such as nano-sized crystallites, impurities, imperfections, and edges. As shown in Fig. 5, the D-band intensity of GNS gradually increased with the heating rate during exfoliation. The I_D/I_G ratio calculated from the Raman spectra is often used as an indicator of the structure quality of graphene. As shown in Table 1, the I_D/I_G ratio increased monotonously from 1.165 for GNS-1 to 1.354 for GNS-30, and eventually reached 1.872 for the HGNS300 sample. This result was attributed to the increase in the defect sites on the hole edges of graphene.

The contents of residual oxygen functional groups are another factor that might affect the microwave absorption ability of RGOs. To compare the amount of these groups in the four different graphene samples, their C and O contents were measured by EA, and the results are listed in Table 1. Since all four samples were reduced at the same temperature (300 °C), their C/O ratios were very close despite the different heating rates.

Also shown in Table 1 is the SSA measured by the BET method. The sample reduced at the lowest heating rate (GNS300-1) had the lowest SSA of 399 m^2/g. In contrast, HGNS300, which was reduced ultra-rapidly, showed the highest SSA of 636 m^2/g. This highest SSA of HGNS300 might be attributed to its high degree of exfoliation as well as its rough surface morphology, which can effectively prevent restacking.

3.2. Measurements of microwave characteristics

To determine the microwave characteristics of the composite absorbers, their complex relative permittivity ($\varepsilon_r = \varepsilon' - j\varepsilon''$) and permeability ($\mu_r = \mu' - j\mu''$) were then measured with the FSMM system in the range of 3–18 GHz. These curves of ε_r and μ_r can be utilized to theoretically simulate the RL vs. frequency. Alternatively, the real RL curves for an absorber sheet can be directly measured with the same FSMM system. Both methods were performed in this study and the results were compared in order to cross-check the validity of theoretical simulation. Fig. 6 (a) and (b) display, respectively, the measured real (ε') and imaginary (ε'') parts of the

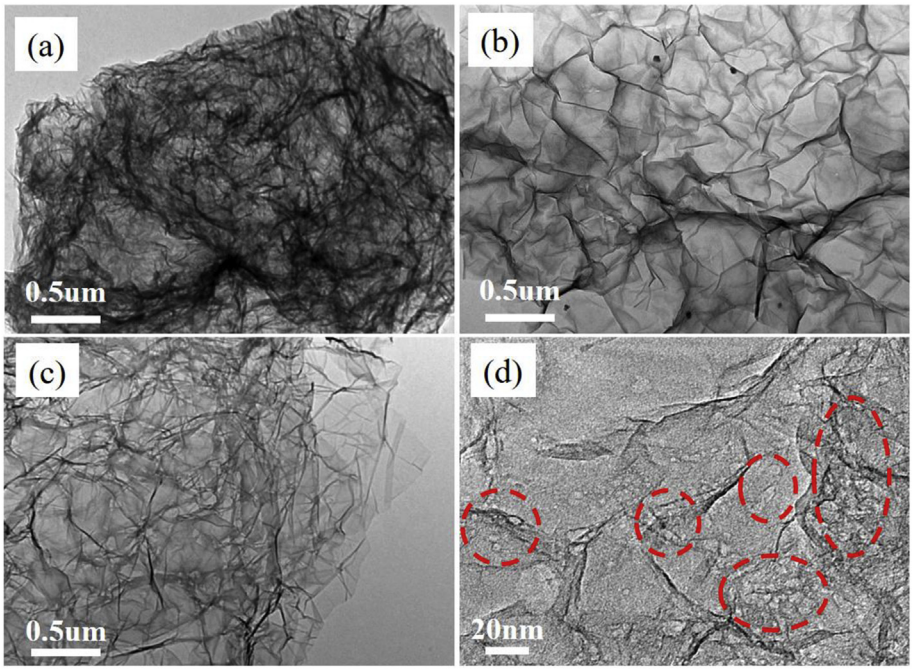

Fig. 3. The TEM images of (a) GNS300-1, (b) GNS300-10, (c) GNS300-30, and (d) HGNS300. The red circles in (d) indicate the areas containing holes. (For interpretation of the references to colour in this figure legend, the reader is referred to the web version of this article.)

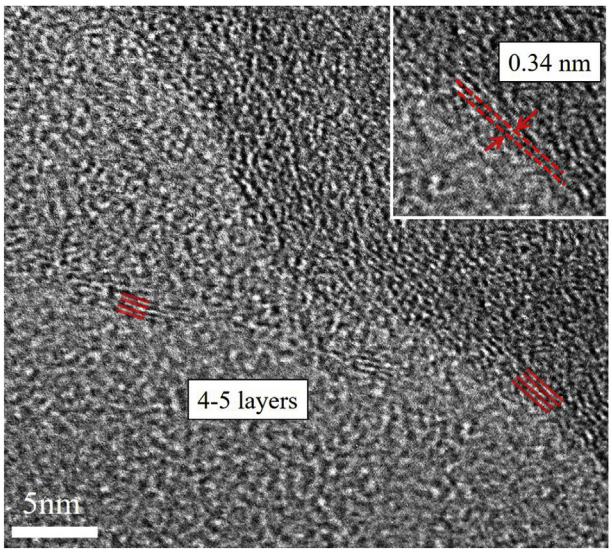

Fig. 4. HR-TEM image of HGNS300. The number of atomic layers are indicated by the red lines. The inset shows the spacing (0.34 nm) between atomic layers. (For interpretation of the references to colour in this figure legend, the reader is referred to the web version of this article.)

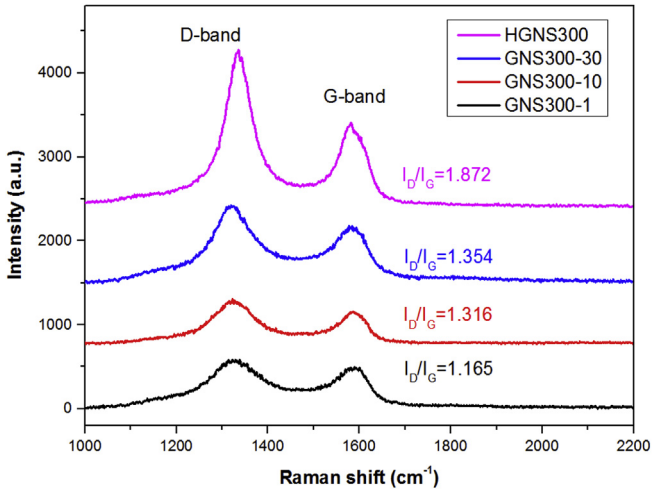

Fig. 5. Raman spectra of GNS300-1, GNS300-10, GNS300-30, and HGNS300 samples.

Table 1
Raman analysis, elemental analysis, and BET surface area analysis of GNS and HGNS samples.

	I_D/I_G[a]	C (at.%)[b]	O (at.%)[b]	C/O	SSA (m^2/g)[c]
GNS300-1	1.165	78.4	21.5	3.64	399
GNS300-10	1.316	80.5	19.4	4.15	544
GNS300-30	1.354	77.1	22.8	3.38	528
HGNS300	1.872	77.9	21.9	3.56	636

[a] The intensity ratio of D-band to G-band on Raman spectrum.
[b] From elemental analysis.
[c] BET specific surface area.

relative permittivity for all of the 1-wt.% microwave absorbing composites. With GNS300s, HGNS300, and silicone rubber being non-magnetic, all of the composite absorbers had a μ' value of ~1 and a negligible μ'' (not shown). Consequently, their microwave absorbing capability should derive from the electric losses only.

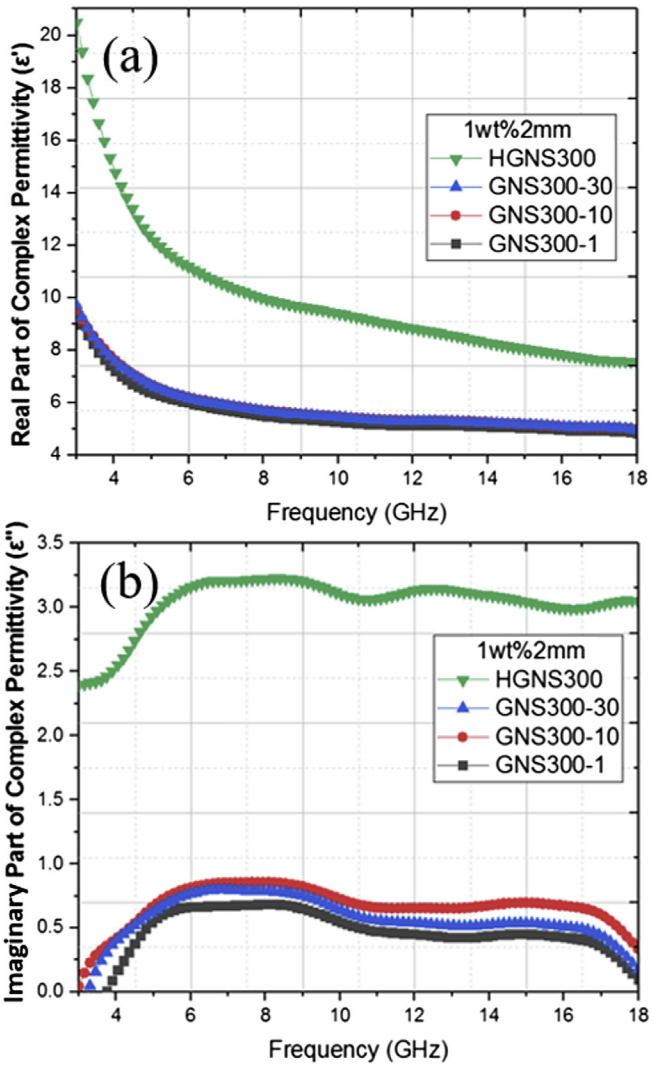

Fig. 6. Dispersion curves of the (a) real and (b) imaginary parts of the relative permittivity for composites with 1 wt.% of GNS or HGNS fillers.

Neat silicone rubber (not shown) has an ε' value of ~3 and a negligible ε'' (3–18 GHz).

ε' and ε'' are associated with the storage and dissipation of electric energy, respectively. As shown in Fig. 6 (a) and (b), HGNS300 performed much better in terms of both ε' and ε'' than all other GNS300 samples at 1 wt.% loading. Its ε' values ranged between 7.7 and 20.6, and its ε'', which is a critical factor for the absorber performance, was in the range 2.3–3.2. Note that excessively large ε' and ε'' would cause high surface reflection due to a large impedance mismatch between air and the dielectric. The permittivity values for our HGNS300/silicone rubber composite lie within the range of acceptable impedance mismatch. For example, similar non-magnetic dielectric microwave absorbers have been studied in Refs. [21,23,24,30,80], and their permittivity values roughly lie within this range for the optimized performances.

Fig. 7 displays the dielectric loss tangents $\tan\delta_\varepsilon$ ($=\varepsilon''/\varepsilon'$) for all of the composites. Clearly HGNS300 exhibited a larger $\tan\delta_\varepsilon$ than the other GNS samples, confirming that it had a higher dielectric loss than the others. Moreover, its dielectric loss covered a wide frequency range (its loss tangent was greater than 0.2 from 4 to 18 GHz).

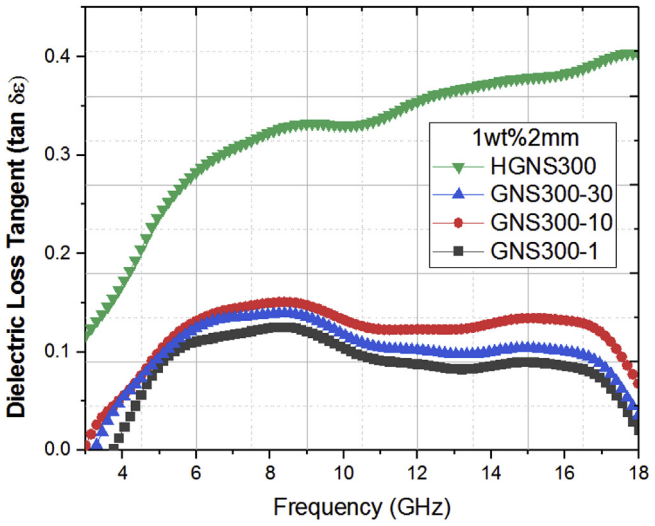

Fig. 7. Dielectric loss tangents for all specimens.

Fig. 8 depicts the experimental RL vs. frequency curves, obtained from direct measurement with the FSMM system, of all the composite sheets (2 mm thick) containing 1 wt.% of various graphene. RL (dB) is defined by: RL = 10 $\log_{10}P_r/P_i$, where P_r and P_i are the measured powers of the incident and reflected microwaves. All specimens except HGNS300 exhibited similar RL curves with a minimum of −7.9 to −8.3 dB at 16.5 GHz. These RL values are actually quite good considering that the loading level is so low. However, merely 1 wt.% of HGNS300 can offer an extraordinarily good RL of −32.1 dB at 13.2 GHz, and the bandwidth of RL less than −10 dB (equivalent to 90% absorption [35,81,82]) was as large as 5 GHz (from 11.3 to 16.3 GHz). These results suggest that the holey structure can significantly improve the microwave absorbing performance of graphene.

The minimum value of RL and the resonance frequency can be adjusted by altering the absorber thickness. Theoretically, the RL at normal incidence for an absorber layer with thickness, d, backed by a conductor can be calculated from the measured complex ε_r and μ_r versus frequency, f, by exploiting the following formula [77]:

$$\mathrm{RL(dB)} = 20\log\left|\frac{z_{in}-1}{z_{in}+1}\right|,$$

where z_{in} is the normalized input impedance of the absorber sheet backed by an ideal conductor. z_{in} is defined as

$$z_{in} = \sqrt{\frac{\mu_r}{\varepsilon_r}}\tanh\left[j\left(\frac{2\pi fd}{c}\right)\sqrt{\mu_r\varepsilon_r}\right],$$

where c is the speed of light in free space.

The calculated theoretical RL curves for the composite filled with 1 wt.% of HGNS300 with various thicknesses are depicted in Fig. 9. We may compare the theoretical RL curve for thickness d = 2.0 mm (pink circles) with the corresponding experimentally measured RL curve (pink triangles, the one for 1 wt.% HGNS300) in Fig. 8. Given the complexity of an EM absorption characterization system, the theoretical and experimental RL curves matched quite well in the trend, value, and resonant frequency. Fig. 9 clearly shows that, as the thickness (d) increased, the absorption resonance downshifted towards lower frequencies. At d = 3.0 mm, an optimal RL of −45.3 dB was obtained at 7.8 GHz, and the absorption bandwidth (for RL less than −10 dB, i.e., 90% absorption) amounted up to 3.2 GHz (from 6.5 to 9.7 GHz). Fig. 9 also suggests that EM absorbers for a wide microwave frequency range—from 5 to 18 GHz—can be fabricated using this composite material with d = 2–4 mm. Given such a low content of microwave absorbing fillers, these RL values and bandwidths of the composite absorber are truly remarkable.

High-temperature post annealing can further remove the residual oxygen functional groups on graphene, and consequently may change its microwave absorption properties. To investigate this effect, we used three different temperatures (300, 700, and 1100 °C) to prepare annealed HGNS300 samples, which were named HGNS300→300, HGNS300→700, and HGNS300→1100, respectively. The Raman spectra of the annealed samples are shown in Fig. S1 (supplementary content). Their I_D/I_G ratios (listed in Table S1) were nearly the same because the lattice defects were hardly affected at these temperatures. In contrast, the C/O atomic ratio (also listed in Table S1) increased drastically (from 4.8 to 44.5) with increasing annealing temperature due to the removal of oxygen functional groups. Table S1 also reveals that the BET surface

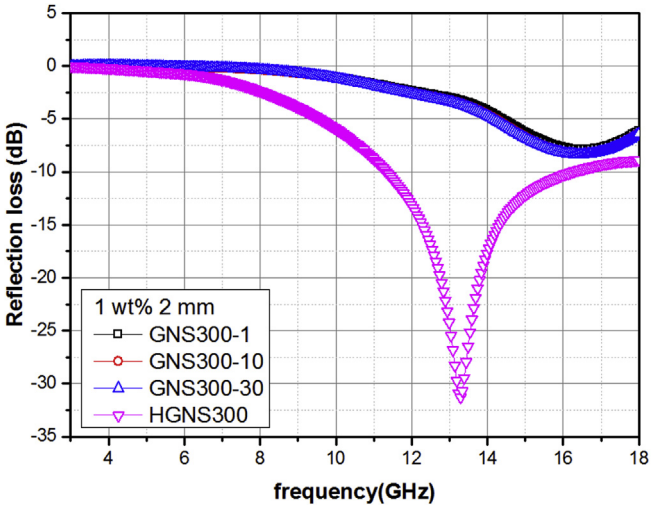

Fig. 8. Experimentally measured RL vs. frequency for composites with 1 wt.% of GNS or HGNS fillers at a fixed thickness of 2 mm.

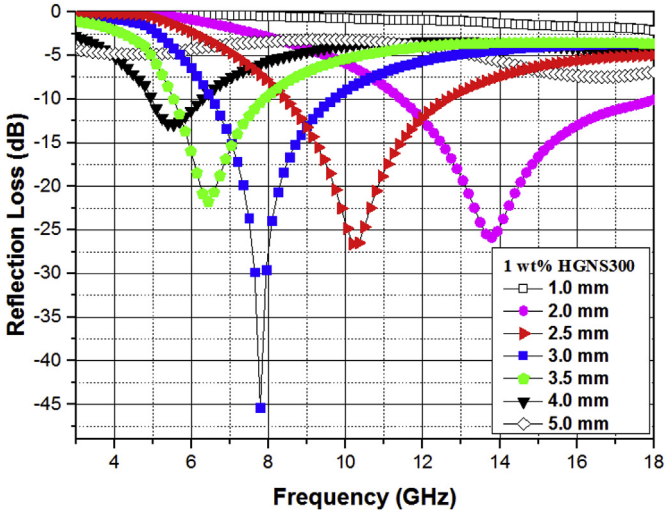

Fig. 9. Calculated RL vs. frequency for the composite with 1 wt.% of HGNS300 at different thicknesses.

area of HGNS300 was not affected by annealing. The measured RL vs. frequency curves for the 2-mm-thick composites filled with 1 wt.% of HGNS300→300, HGNS300→700, or HGNS300→1100 are displayed in Fig. S2. All three absorbers exhibited good microwave absorption properties with slight differences. Compared to HGNS300→300, HGNS300→1100 had a slightly better minimum RL (−32.3 dB) at a lower frequency (12.6 GHz) with a smaller bandwidth (4 GHz), whereas HGNS300→700 had a higher minimum RL (−23.1 dB) at the same frequency (13.2 GHz) with a much larger bandwidth (>7.6 GHz). Given the similar BET surface area and defect level, these differences most probably resulted from their distinct amounts of oxygen functional groups, which affected both the dipole relaxation loss and the conductivity of HGNS.

There were two reasons for our choice of such a low loading content at 1 wt.%. First, high-quality well-exfoliated graphene are still quite expensive, so we wished to minimize the amount of graphene without sacrificing the microwave absorption performance. Second, given the large specific surface area of our HGNS300, it was not easy to attain uniform dispersion in silicone rubber. As the loading content increased, the viscosity of the mixture increased rapidly, indicating poorer dispersion of the nano-fillers in the matrix. Nevertheless, 2-mm-thick composite absorber sheets with 1.5 and 2 wt.% of HGNS300 were fabricated and their microwave absorption performances were measured. Their RL vs. frequency curves are displayed in Figs. S3 and S4 (supplementary content). Both of them were also very effective absorbers in X-band and Ku-band, although their RL values were slightly higher than those of the 1-wt.%. counterpart (see Fig. 9). This might be attributed to their lower degree of dispersion uniformity and/or impedance mismatch due to the increases in permittivity and conductivity. When the HGNS300 amount was further increased (i.e., above 2 wt.%), the mixture became too viscous to be properly processed by our procedure.

Table 2 uses results from the literature and this work to compare the key performance indicators for composites incorporating graphene or graphene-containing hybrid fillers at various loading levels, including the minimum RL, central frequency, and bandwidth. As can be seen, our HGNS300 surpassed all the others at 1 wt.% loading. Amazingly, our results can even rival the most sophisticated composite absorbers using dielectric/magnetic hybrid fillers (i.e., graphene decorated, coated, or mixed with magnetic or dielectric particles), which have loading contents much higher than 1 wt.%. The low filler loading level required to achieve high performance implies that lightweight microwave absorber sheets can be fabricated, which will be very attractive in many applications. Furthermore, because high-quality graphene products are still quite expensive, a low loading content is very advantageous for practical applications from the point of view of fabrication cost.

3.3. Microwave absorbing mechanisms of holey graphene

Table 2 reveals that it is quite uncommon that such a good performance can be obtained with only 1 wt.% filler loading. To understand the key mechanism for the excellent microwave absorption of HGNS300, we should examine all kinds of loss mechanisms. With silicone rubber and graphene both being non-magnetic, the microwave absorption must derive entirely from dielectric losses and/or conductive dissipation. Table 3 listed the resistivity values of the composite absorbers measured with an ultra-high resistance meter (Hioki, SM-8200 Digital Super Megohmmeter). As 1 wt.% filler loading was below the percolation threshold, all the composites were virtually non-conductive. This allows us to neglect the absorption caused by conductive dissipation and focus on dielectric losses.

Dielectric losses can be attributed to a number of possible sources, including dipolar polarization, interfacial or Maxwell-Wagner-Sillars (MWS) polarization effect, defect-induced polarization or loss, oxygen functional groups on the surface of graphene. Many researchers [22,35,36,74,83] have reported extra dipole relaxation offered by residual oxygen functional groups, which create losses in the electric field due to the twisting and vibrating of the permanent electric dipoles. But since the four samples were all reduced at the same temperature of 300 °C, they had similar oxygen contents (see Table 1). Thus it is unlikely that oxygen functional

Table 3
Resistivity (ρ) of silicone rubber composites filled with various GNSs or HGNS.

Filler type	Loading content (wt.%)	ρ (Ω-cm)
GNS300-1	1	$>1.5*10^{15}$[a]
GNS300-10	1	$>1.5*10^{15}$
GNS300-30	1	$>1.5*10^{15}$
HGNS300	1	$2.3*10^{13}$

[a] The upper limit of our measurement equipment.

Table 2
Microwave absorber performances at 2–18 GHz using various graphene fillers or hybrid fillers made of graphene decorated or mixed with other materials.[a]

Filler type	Matrix type	Filler loading (wt.%)	Minimum RL (dB)	Frequency & bandwidth[b] (GHz, GHz)	Refs.
Holey graphene	Silicone rubber	1	−45.3	(7.8, 3.2)	This work
RGO (Hummers)	Poly-(ethylene oxide)	~4.2 (2.6 vol.%)	−38.8	(16.5, 4.1)	[21]
		~0.9 (0.54 vol.%)	−16	(7.1, ~2.5)	
RGO (Hummers)	Not mentioned	Not mentioned	−6.9	(7, 0)	[22]
RGO (Hummers)	Nitrile butadiene rubber	2	~ −10	(~10.3, 0)	[23]
		4	~ −17	(~11.5, >2)	
		10	−57	(9.6, 4.5)	
RGO (Staudenmaier)	Silicone rubber	1	−37.8	(12.3, 4.8)	[30]
RGO	Poly (dimethyl siloxane)	5	−14	(11.5, ~3)	[25]
Acid-modified RGO	Thermoplastic polyurethane	10	−12.6	(10.4, ~0.3)	[24]
CNTs/RGO	Poly (dimethyl siloxane)	5	−55	(10.1, 3.5)	[25]
$NiFe_2O_4$/RGO	Paraffin	70	−42	(6.6, ~2.8)	[40]
Fe_3O_4/RGO	Paraffin	50	−44.6	(6.6, 2)	[35]
Hematite/RGO	Paraffin	15	−78	(15.4, >6.7)	[36]
α-Fe/RGO	Paraffin	40	−45	(7.5, ~2.5)	[37]
CuS/RGO	Polyvinylidene fluoride	5	−32.7	(10.7, ~3.7)	[38]
Ni/RGO	Paraffin	23	−16.5	(12, >5)	[39]

[a] The results summarized here include only the studies using the configuration of a single-layer absorber.
[b] The frequency range for RL < −10 dB.

groups were the cause for the great differences in RL.

There are two most noticeable features of HGNS300 compared to the other samples: (1) its significantly higher I_D/I_G ratio, which indicated a high density of defects; (2) its extremely high SSA, which might be attributed to its good resistance against restacking as a result of its rough surface morphology and outward-opening hole edges. Consequently, HGNS300's remarkable microwave absorbing performance at such a low loading content might be attributed to the following mechanisms: defect-induced losses, multiple reflection of microwave in between the surfaces of better-exfoliated graphene sheets, and enhanced MWS interfacial polarization.

First of all, high defect density may significantly improve microwave absorption. Several research groups have reported that defects [22,33,35,36,74–76] on the graphene surface are beneficial rather than harmful for microwave absorption applications because they offer extra loss mechanisms. Watts et al. [76] have found that defective CNTs displayed higher permittivity than graphitic CNTs because the defects acted as polarization centers, which would cause losses under the altering EM field. For our HGNS300, on the edges of numerous holes, there are plenty of dangling bonds and unsaturated coordination, which might give rise to orientational polarization [74]. Belavin et al. [84] have also reported that lattice defects on CNTs can create localized states near the Fermi level, and incident EM energy can be absorbed by the transition from contiguous states to the Fermi level [76]. Theoretical calculations have predicted that on the zigzag edges of graphene nanoribbons, RGO, and nanographite, in the proximity of the Fermi level, lies a localized edge state [85,86], whose existence were verified experimentally by near-edge x-ray absorption fine-structure spectrum [87–90] as well as ultraviolet photoelectron spectrum [88]. Transition from the top of the valence band into the edge state by absorbing a microwave photon is allowed quantum mechanically because of the nonzero transition matrix element and the little energy required for this process. The abundant edge sites around the holes on our HGNS may offer many such edge-derived states, which can enhance absorption of microwave.

Secondly, multiple reflections and scattering of microwave between the graphene sheets can considerably lengthen the absorption paths and hence increase the microwave absorption [22,23,32,83]. The highest SSA of HGNS300 as well as its anti-restacking property resulted in more interfaces between HGNS and the matrix, leading to enhanced multiple reflections. Moreover, the numerous hole edges increased the scattering effect significantly.

Thirdly, the MWS interfacial polarization effect can offer additional dielectric loss [25,35,36,74,81,83,91]. The highest degree of exfoliation of HGNS led to the largest area of filler-matrix interfaces, which gave rise to strong MWS effect. This polarization effect was caused by the accumulation of graphene's delocalized electrons at the HGNS-silicone rubber interface when they were driven by the applied electric field. While MWS effect is usually observed in the MHz range or below, in composites filled with nanocarbon-based additives, such as CNT/graphene [25], Fe_3O_4/RGO [35], Ag/RGO [91], and graphene nanoribbons [83], many researchers have identified its presence at GHz frequencies. These possible microwave absorption mechanisms in our HGNS300 composite absorber are schematically illustrated in Fig. 10.

Many researchers [25,35,36,38,74,83] have reported that the number of relaxation mechanisms in a dielectric material is reflected in the number of semicircle segments on the $\varepsilon'-\varepsilon''$ curve, or the Cole-Cole plot [92]. In Fig. 11, the Cole-Cole plot for the 1-wt.% HGNS300 composite absorber reveals the presence of three overlapping semicircles, suggesting that there were three dielectric loss mechanisms involved in its microwave absorption. This supports our speculation of the three aforementioned mechanisms in our composite absorber.

We believe the three loss mechanisms, namely, high defect density, increased multiple reflections and scattering, and enhanced MWS effect, jointly brought about the high RL and large absorption bandwidth for HGNS300 at 1 wt.% loading.

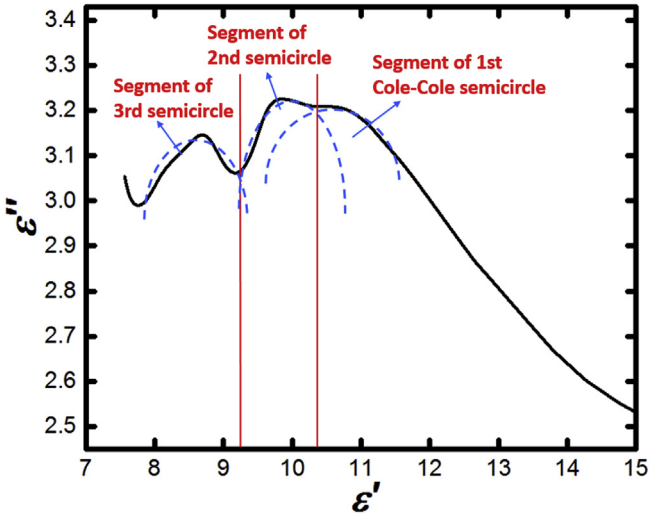

Fig. 11. Cole-Cole plot for the 1-wt.% HGNS300 composite absorber.

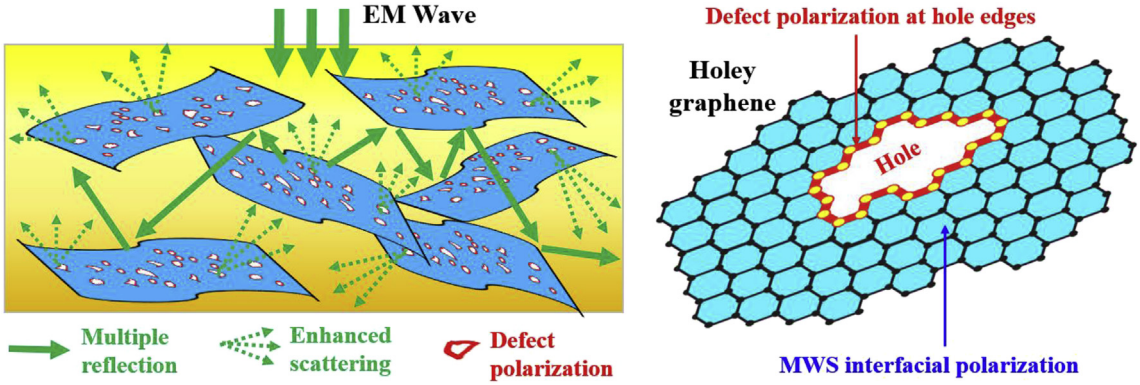

Fig. 10. Schematic of possible microwave absorption mechanisms in HGNS.

4. Conclusions

A comparison of the microwave absorption performance of silicone rubber absorbers filled with various graphene products produced by reducing GO with different heating rates was made. Holey graphene (HGNS300) prepared by a facile ultra-rapid heating method exhibited considerably higher increases in the dielectric permittivity, as well as RL improvements over the other graphene samples prepared at lower heating rates. With a very low loading level (1 wt.%) of HGNS300, the experimentally measured RL was as low as −32.1 dB at 13.2 GHz for an absorber thickness of 2.0 mm. The bandwidth (RL < 10 dB) of this absorber sheet was as wide as 5.0 GHz (from 11.3 to 16.3 GHz). Moreover, calculations revealed that an optimum RL of −45.3 dB can be attained at 7.8 GHz using a thickness of 3.0 mm. Comparison was made among the material properties of all samples, including surface morphology, Raman spectrum, C/O ratio, and SSA, in order to determine the causes leading to the extraordinary performance of HGNS300 at such a low loading level. The results indicated that HGNS300 possessed the highest density of defects and the largest SSA. The largest SSA indicated that it had the highest degree of exfoliation as well as the best anti-restacking ability, which was probably due to its roughest surface morphology and the outward opening hole edges. Consequently, defect-induced losses combined with the increased multiple reflections/scattering and MWS interfacial polarization resulted in the significantly enhanced microwave absorption. The holey graphene microwave absorber shows great potential for practical applications, given the low processing cost and the low filler loading required for high performance.

Acknowledgements

This study is sponsored by Ministry of Science and Technology of Taiwan under Grants No. MOST-105-2221-E-155-017, MOST-106-2623-E-606-003-D, and MOST-106-2221-E-155-016, National Defense Industrial Development Foundation, and Chemical System Research Division at National Chung Shan Institute of Science and Technology under Grant No. XD05011P-CS.

Appendix A. Supplementary data

Supplementary data related to this article can be found at https://doi.org/10.1016/j.compositesb.2017.10.001.

References

[1] Liu X, Zhang Z, Wu Y. Absorption properties of carbon black/silicon carbide microwave absorbers. Compos Part B 2011;42:326–9.
[2] Li WP, Zhu LQ, Gu J, Liu HC. Microwave absorption properties of fabric coated absorbing material using modified carbonyl iron power. Compos Part B 2011;42:626–30.
[3] Pokharel P, Truong QT, Lee DS. Multi-step microwave reduction of graphite oxide and its use in the formation of electrically conductive graphene/epoxy composites. Compos Part B 2014;64:187–93.
[4] Wu W, Zhai Y, Zhang Y, Ren W. Mechanical and microwave absorbing properties of in situ prepared hydrogenated acrylonitrile–butadiene rubber/rare earth acrylate composites. Compos Part B 2014;56:497–503.
[5] Liu Y, Song D, Wu C, Leng J. EMI shielding performance of nanocomposites with MWCNTs, nanosized Fe_3O_4 and Fe. Compos Part B 2014;63:34–40.
[6] Joshi A, Bajaj A, Singh R, Anand A, Alegaonkar PS, Datar S. Processing of graphene nanoribbon based hybrid composite for electromagnetic shielding. Compos Part B 2015;69:472–7.
[7] Tang H, Jian X, Wu B, Liu S, Jiang Z, Chen X, et al. Fe_3C/helical carbon nanotube hybrid: facile synthesis and spin induced enhancement in microwave-absorbing properties. Compos Part B 2016;107:51–8.
[8] Al-Ghamdi AA, Al-Hartomy OA, Al-Solamy FR, Dishovsky N, Malinova P, Atanasova G, et al. Conductive carbon black/magnetite hybrid fillers in microwave absorbing composites based on natural rubber. Compos Part B 2016;96:231–41.
[9] Wu J, Chen J, Zhao Y, Liu W, Zhang W. Effect of electrophoretic condition on the electromagnetic interference shielding performance of reduced graphene oxide-carbon fiber/epoxy resin composites. Compos Part B 2016;105:167–75.
[10] Bibi M, Abbas SM, Ahmad N, Muhammad B, Iqbal Z, Rana UA, et al. Microwaves absorbing characteristics of metal ferrite/multiwall carbon nanotubes nanocomposites in X-band. Compos Part B 2017;114:139–48.
[11] Mondal S, Ganguly S, Das P, Khastgir D, Das NC. Low percolation threshold and electromagnetic shielding effectiveness of nano-structured carbon based ethylene methyl acrylate nanocomposites. Compos Part B 2017;119:41–56.
[12] Galindo B, Benedito A, Gimenez E, Compañ V. Comparative study between the microwave heating efficiency of carbon nanotubes versus multilayer graphene in polypropylene nanocomposites. Compos Part B 2016;98:330–8.
[13] Chen Y, Zhang A, Ding L, Liu Y, Lu H. A three-dimensional absorber hybrid with polar oxygen functional groups of MWNTs/graphene with enhanced microwave absorbing properties. Compos Part B 2017;108:386–92.
[14] Lee SE, Choi O, Hahn HT. Microwave properties of graphite nanoplatelet/epoxy composites. J Appl Phys 2008;104(3):033705.
[15] Micheli D, Vricella A, Pastore R, Marchetti M. Synthesis and electromagnetic characterization of frequency selective radar absorbing materials using carbon nanopowders. Carbon 2014;77:756–74.
[16] Wu KH, Ting TH, Wang GP, Ho WD, Shih CC. Effect of carbon black content on electrical and microwave absorbing properties of polyaniline/carbon black nanocomposites. Polym Degrad Stab 2008;93(2):483–8.
[17] Vinayasree S, Soloman MA, Sunny V, Mohanan P, Kurian P, Anantharaman MR. A microwave absorber based on strontium ferrite–carbon black–nitrile rubber for S and X-band applications. Compos Sci Technol 2013;82:69–75.
[18] Kim JB, Lee SK, Kim CG. Comparison study on the effect of carbon nano materials for single-layer microwave absorbers in X-band. Compos Sci Technol 2008;68(14):2909–16.
[19] Qing Y, Wang X, Zhou Y, Huang Z, Luo F, Zhou W. Enhanced microwave absorption of multi-walled carbon nanotubes/epoxy composites incorporated with ceramic particles. Compos Sci Technol 2014;102:161–8.
[20] Bhattacharya P, Sahoo S, Das CK. Microwave absorption behaviour of MWCNT based nanocomposites in X-band region. Express Polym Lett 2013;7(3):212–23.
[21] Bai X, Zhai Y, Zhang Y. Green approach to prepare graphene-based composites with high microwave absorption capacity. J Phys Chem C 2011;115(23):11673–7.
[22] Wang C, Han X, Xu P, Zhang X, Du Y, Hu S, et al. The electromagnetic property of chemically reduced graphene oxide and its application as microwave absorbing material. Appl Phys Lett 2011;98(7):072906.
[23] Singh VK, Shukla A, Patra MK, Saini L, Jani RK, Vadera SR, et al. Microwave absorbing properties of a thermally reduced graphene oxide/nitrile butadiene rubber composite. Carbon 2012;50(6):2202–8.
[24] Bhattacharya P, Das CK, Kalra SS. Graphene and MWCNT: potential candidate for microwave absorbing materials. J Mater Sci Res 2012;1(2):126–32.
[25] Kong L, Yin X, Zhang Y, Liu X, Cheng L, Zhang L. Electromagnetic wave absorption properties of graphene modified with carbon nanotube/poly(-dimethyl siloxane) composites. Carbon 2014;73:185–93.
[26] Gogoi JP, Bhattacharyya NS, Raju KCJ. Synthesis and microwave characterization of expanded graphite/novolac phenolic resin composite for microwave absorber applications. Compos Part B 2011;42:1291–7.
[27] Cao MS, Song WL, Hou ZL, Wen B, Yuan J. The effects of temperature and frequency on the dielectric properties, electromagnetic interference shielding and microwave-absorption of short carbon fiber/silica composites. Carbon 2010;48:788–96.
[28] Cao MS, Yang J, Song WL, Zhang DQ, Wen B, Jin HB, et al. Ferroferric oxide/multiwalled carbon nanotube vs polyaniline/ferroferric oxide/multiwalled carbon nanotube multiheterostructures for highly effective microwave absorption. ACS Appl Mater Interfaces 2012;4(12):6949–56.
[29] Lu MM, Cao MS, Chen YH, Cao WQ, Liu J, Shi HL, et al. Multiscale Assembly of grape-like ferroferric oxide and carbon-nanotubes: a smart absorber prototype varying temperature to tune intensities. ACS Appl Mater Interfaces 2015;7(34):19408–15.
[30] Chen CY, Pu NW, Liu YM, Huang SY, Wu CH, Ger MD, et al. Remarkable microwave absorption performance of graphene at a very low loading ratio. Compos Part B 2017;114:395–403.
[31] Liang J, Wang Y, Huang Y, Ma Y, Liu Z, Cai J, et al. Electromagnetic interference shielding of graphene/epoxy composites. Carbon 2009;47(3):922–5.
[32] Wen B, Wang XX, Cao WQ, Shi HL, Lu MM, Wang G, et al. Reduced graphene oxides: the thinnest and most lightweight materials with highly efficient microwave attenuation performances of the carbon world. Nanoscale 2014;6:5754–61.
[33] Wen B, Cao M, Lu M, Cao W, Shi H, Liu J, et al. Reduced graphene oxides: light-weight and high-efficiency electromagnetic interference shielding at elevated temperatures. Adv Mater 2014;26(21):3484–9.
[34] Cao WQ, Wang XX, Yuan J, Wang WZ, Cao MS. Temperature dependent microwave absorption of ultrathin graphene composites. J Mater Chem C 2015;3(38):10017–22.
[35] Zong M, Huang Y, Zhao Y, Sun X, Qu C, Luo D, et al. Facile preparation, high microwave absorption and microwave absorbing mechanism of RGO–Fe_3O_4 composites. RSC Adv 2013;3(45):23638–48.
[36] Chen D, Wang GS, He S, Liu J, Guo L, Cao MS. Controllable fabrication of monodispersed RGO-hematite nanocomposites and their enhanced wave absorption properties. J Mater Chem A 2013;1:5996–6003.
[37] Zhao X, Zhang Z, Wang L, Xi K, Cao Q, Wang D, et al. Excellent microwave

absorption property of graphene-coated Fe nanocomposites. Sci Rep 2013;3:3421.
[38] Zhang XJ, Wang GS, Wei YZ, Guo L, Cao MS. Polymer-composite with high dielectric constant and enhanced absorption properties based on graphene-CuS nanocomposites and polyvinylidene fluoride. J Mater Chem A 2013;1:12115–22.
[39] Fang JJ, Li SF, Zha WK, Cong HY, Chen JF, Chen ZZ. Microwave absorbing properties of nickel-coated graphene. J Inorg Mater 2011;26(5):467–71.
[40] He JZ, Wang XX, Zhang YL, Cao MS. Small magnetic nanoparticles decorating reduced graphene oxides to tune the electromagnetic attenuation capacity. J Mater Chem C 2016;4:7130–40.
[41] Wang C, Li D, Too CO, Wallace GG. Electrochemical properties of graphene paper electrodes used in lithium batteries. Chem Mater 2009;21(13):2604–6.
[42] Abouimrane A, Compton OC, Amine K, Nguyen ST. Non-annealed graphene paper as a binder-free anode for lithium-ion batteries. J Phys Chem 2010;114(29):12800–4.
[43] Stoller MD, Park S, Zhu Y, An J, Ruoff RS. Graphene-based ultracapacitors. Nano Lett 2008;8(10):3498–502.
[44] Peng YY, Liu YM, Chang JK, Wu CH, Ger MD, Pu NW, et al. A facile approach to produce holey graphene and its application in supercapacitors. Carbon 2015;81:347–56.
[45] Mao S, Wen Z, Kim H, Lu G, Hurley P, Chen J. A general approach to one-pot fabrication of crumpled graphene-based nanohybrids for energy applications. ACS Nano 2012;6(8):7505–13.
[46] Luo J, Zhao X, Wu J, Jang HD, Kung HH, Huang J. Crumpled graphene-encapsulated Si nanoparticles for lithium ion battery anodes. J Phys Chem Lett 2012;3(13):1824–9.
[47] Luo J, Jang HD, Huang J. Effect of sheet morphology on the scalability of graphene-based ultracapacitors. ACS Nano 2013;7(2):1464–71.
[48] Xi K, Kidambi PR, Chen R, Gao C, Peng X, Ducati C, et al. Binder free three-dimensional sulphur/few-layer graphene foam cathode with enhanced high-rate capability for rechargeable lithium sulphur batteries. Nanoscale 2014;6:5746–53.
[49] Zhang H, Yu X, Braun PV. Three-dimensional bicontinuous ultrafast-charge and -discharge bulk battery electrodes. Nat Nanotechnol 2011;6:277–81.
[50] Wu CH, Pu NW, Wu PJ, Peng YY, Shih CN, Chen CY, et al. High-electrical-resistivity thermally-conductive phase change materials prepared by adding nanographitic fillers into paraffin. Microelectron Eng 2015;138:91–6.
[51] Zhao X, Hayner CM, Kung MC, Kung HH. In-plane vacancy-enabled high-power Si–graphene composite electrode for lithium-ion batteries. Adv Energy Mater 2011;1(6):1079–84.
[52] Wu ZS, Ren W, Wen L, Gao L, Zhao J, Chen Z, et al. Graphene anchored with Co_3O_4 nanoparticles as anode of lithium ion batteries with enhanced reversible capacity and cyclic performance. ACS Nano 2010;4(6):3187–94.
[53] Xing L, Cui C, Ma C, Xue X. Facile synthesis of α-MnO_2/graphene nanocomposites and their high performance as lithium-ion battery anode. Mater Lett 2011;65(14):2104–6.
[54] Zhu X, Zhu Y, Murali S, Stoller MD, Ruoff RS. Nanostructured reduced graphene oxide/Fe_2O_3 composite as a high-performance anode material for lithium ion batteries. ACS Nano 2011;5(4):3333–8.
[55] Zhao B, Ma C, Liang L, Guo W, Fan B, Guo X, et al. An impedance match method used to tune the electromagnetic wave absorption properties of hierarchical ZnO assembled by porous nanosheets. CrystEngComm 2017;19:3640–8.
[56] Zhao B, Zhao W, Shao G, Fan B, Zhang R. Corrosive synthesis and enhanced electromagnetic absorption properties of hollow porous Ni/SnO_2 hybrids. Dalton Trans 2015;44:15984–93.
[57] Zhao B, Guo X, Zhou Y, Su T, Ma C, Zhang R. Constructing hierarchical hollow CuS microspheres via a galvanic replacement reaction and their use as wide-band microwave absorbers. CrystEngComm 2017;19:2178–86.
[58] Zhao B, Fan B, Xu Y, Shao G, Wang X, Zhao W, et al. Preparation of honeycomb SnO_2 foams and configuration-dependent microwave absorption features. ACS Appl Mater Interfaces 2015;7:26217–25.
[59] Zhao B, Shao G, Fan B, Zhao W, Xie Y, Zhang R. Synthesis of flower-like CuS hollow microspheres based on nanoflakes self-assembly and their microwave absorption properties. J Mater Chem A 2015;3:10345–52.
[60] Zhao B, Guo X, Zhao W, Deng J, Shao G, Fan B, et al. Yolk–shell Ni@SnO_2 composites with a designable interspace to improve the electromagnetic wave absorption properties. ACS Appl Mater Interfaces 2016;8:28917–25.
[61] Zhao B, Guo X, Zhao W, Deng J, Fan B, Shao G, et al. Facile synthesis of yolk–shell Ni@void@SnO2(Ni_3Sn_2) ternary composites via galvanic replacement/Kirkendall effect and their enhanced microwave absorption properties. Nano Res 2017;10(1):331–43.
[62] Zhang Y, Huang Y, Zhang T, Chang H, Xiao P, Chen H, et al. Broadband and tunable high-performance microwave absorption of an ultralight and highly compressible graphene foam. Adv Mater 2015;27(12):2049–53.
[63] Chen Z, Xu C, Ma C, Ren W, Cheng HM. Lightweight and flexible graphene foam composites for high-performance electromagnetic interference shielding. Adv Mater 2013;25(9):1296–300.
[64] Zhao D, Wang L, Yu P, Zhao L, Tian C, Zhou W, et al. From graphite to porous graphene-like nanosheets for high rate lithium-ion batteries. Nano Res 2015;8(9):2998–3010.
[65] Cao H, Zhou X, Zheng C, Liu Z. Metal etching method for preparing porous graphene as high performance anode material for lithium-ion batteries. Carbon 2015;89:41–6.
[66] Zhao X, Hayner CM, Kung MC, Kung HH. Flexible holey graphene paper electrodes with enhanced rate capability for energy storage applications. ACS Nano 2011;5(11):8739–49.
[67] Fang Y, Lv Y, Che R, Wu H, Zhang X, Gu D, et al. Two-dimensional mesoporous carbon nanosheets and their derived graphene nanosheets: synthesis and efficient lithium ion storage. J Am Chem Soc 2013;135(4):1524–30.
[68] Sun L, Tian C, Li M, Meng X, Wang L, Wang R, et al. From coconut shell to porous graphene-like nanosheets for high-power supercapacitors. J Mater Chem A 2013;1:6462–70.
[69] Xu Y, Chen CY, Zhao Z, Lin Z, Lee C, Xu X, et al. Solution processable holey graphene oxide and its derived macrostructures for high-performance supercapacitors. Nano Lett 2015;15(7):4605–10.
[70] Ding B, Yuan C, Shen L, Xu G, Nie P, Lai Q, et al. Chemically tailoring the nanostructure of graphene nanosheets to confine sulfur for high-performance lithium-sulfur batteries. J Mater Chem A 2013;1:1096–101.
[71] Sui ZY, Meng QH, Li JT, Zhu JH, Cui Y, Han BH. High surface area porous carbons produced by steam activation of graphene aerogels. J Mater Chem A 2014;2:9891–8.
[72] Pan D, Wang S, Zhao B, Wu M, Zhang H, Wang Y, et al. Li storage properties of disordered graphene nanosheets. Chem Mater 2009;21:3136–42.
[73] Wang H, Zhang C, Liu Z, Wang L, Han P, Xu H, et al. Nitrogen-doped graphene nanosheets with excellent lithium storage properties. J Mater Chem 2011;21:5430–4.
[74] Wang GS, Zhang XJ, Wei YZ, He S, Guo L, Cao MS. Polymer composites with enhanced wave absorption properties based on modified graphite and polyvinylidene fluoride. J Mater Chem A 2013;1:7031–6.
[75] Zhang XF, Dong XL, Huang H, Wang DK, Lv B, Lei JP. High permittivity from defective carbon-coated Cu nanocapsules. Nanotechnology 2007;18(27):275701.
[76] Watts PCP, Hsu WK, Barnes A, Chambers B. High permittivity from defective multiwalled carbon nanotubes in the X-band. Adv Mater 2003;15(7–8):600–3.
[77] Sadasivuni KK, Ponnamma D, Kim J, Thomas S. Graphene-based polymer nanocomposites in electronics. Springer; 2015. p. 307–43.
[78] Ghodgaonkar DK, Ali NA. Microwave nondestructive testing of composite materials using free-space microwave measurement techniques. In: 15th world conference on non-destructive testing, Rome, Italy; 2000. p. 15–21.
[79] McAllister MJ, Li JL, Adamson DH, Schniepp HC, Abdala AA, Liu J, et al. Single sheet functionalized graphene by oxidation and thermal expansion of graphite. Chem Mater 2007;19:4396–404.
[80] Tang N, Zhong W, Au C, Yang Y, Han M, Lin K, et al. Synthesis, microwave electromagnetic, and microwave absorption properties of twin carbon nanocoils. J Phys Chem C 2008;112(49):19316–23.
[81] Wang Y, Wang L, Wu H. Enhanced microwave absorption properties of α-Fe_2O_3-filled ordered mesoporous carbon nanorods. Materials 2013;6(4):1520–9.
[82] Yang Y, Liu X, Yang Y, Xiao W, Li Z, Xue D, et al. Synthesis of nonstoichiometric zinc ferrite nanoparticles with extraordinary room temperature magnetism and their diverse applications. J Mater Chem C 2013;1(16):2875–85.
[83] Gupta TK, Singh BP, Singh VN, Teotia S, Singh AP, Elizabeth I, et al. MnO_2 decorated graphene nanoribbons with superior permittivity and excellent microwave shielding properties. J Mater Chem A 2014;2(12):4256–63.
[84] Belavin VV, Okotrub AV, Bulusheva LG. A study of the influence of structural imperfection on the electronic structure of carbon nanotubes by x-ray spectroscopy and quantum-chemical methods. Phys Solid State 2002;44(4):663–5.
[85] Nakada K, Fujita M, Dresselhaus G, Dresselhaus MS. Edge state in graphene ribbons: nanometer size effect and edge shape dependence. Phys Rev B 1996;54:17954–61.
[86] Maruyama M, Kusakabe K. Theoretical prediction of synthesis methods to create magnetic nanographite. J Phys Soc Jpn 2004;73:656–63.
[87] Joly VLJ, et al. Observation of magnetic edge state in graphene nanoribbons. Phys Rev B 2010;81:245428.
[88] Entani S, Ikeda S, Kiguchi M, Saiki K, Yoshikawa G, Nakai I, et al. Growth of nanographite on Pt(111) and its edge state. Appl Phys Lett 2006;88(15):153126.
[89] Zhan D, Ni Z, Chen W, Sun L, Luo Z, Lai L, et al. Electronic structure of graphite oxide and thermally reduced graphite oxide. Carbon 2011;49:1362–6.
[90] Brandes JA, Cody GD, Rumble D, Haberstroh P, Wirick S, Gelinas Y. Carbon K-edge XANES spectromicroscopy of natural graphite. Carbon 2008;46:1424–34.
[91] Wageh S, He L, Al-Ghamdi AA, Al-Turki YA, Tjong SC. Nano silver-anchored reduced graphene oxide sheets for enhanced dielectric performance of polymer nanocomposites. RSC Adv 2014;4(54):28426–31.
[92] Cole KS, Cole RH. Dispersion and absorption in dielectrics I. Alternating current characteristics. J Chem Phys 1941;9:341–51.